

**Disentangling interferences in the photoelectron momentum distribution from strong-field ionization**T. Wang<sup>1,\*</sup>, Z. Dube<sup>1</sup>, Y. Mi<sup>1</sup>, G. Vampa<sup>1</sup>, D. M. Villeneuve<sup>1</sup>, P. B. Corkum<sup>1</sup>, Xiaojun Liu<sup>2</sup>, and A. Staudte<sup>1,†</sup><sup>1</sup>*Joint Attosecond Laboratory, National Research Council and University of Ottawa, 100 Sussex Drive, Ottawa, Ontario K1A 0R6, Canada*<sup>2</sup>*State Key Laboratory of Magnetic Resonance and Atomic and Molecular Physics, Wuhan Institute of Physics and Mathematics, Innovation Academy for Precision Measurement Science and Technology, Chinese Academy of Sciences, Wuhan 430071, China*

(Received 24 March 2022; accepted 9 June 2022; published 11 July 2022)

Using the semiclassical two-step model for strong-field ionization, we theoretically investigate subcycle interference structures in the photoelectron momentum distribution. Specifically, we focus on the low-momentum fanlike interference structure. Employing a time-variable soft-core Coulomb potential, we demonstrate that the low-momentum interference arises from the interference between drifted and undrifted electrons from opposite direct quarter cycles. We also find that the main scattering in the nuclear Coulomb potential occurs just after ionization. Our findings suggest that the low-momentum region of the photoelectron spectrum is particularly sensitive to the ion potential and thereby offers another path to probe ultrafast electronic structure dynamics.

DOI: [10.1103/PhysRevA.106.013106](https://doi.org/10.1103/PhysRevA.106.013106)**I. INTRODUCTION**

In multiphoton ionization of atoms and molecules by intense multicycle laser pulses the photoelectron wave packets created at each crest of the optical wave interfere with each other, giving rise to a wealth of structures in the observable photoelectron momentum distributions [1–5]. Whereas some of these interferences arise directly from the symmetry of the optical wave driving the electron current, others inherently rely on the scattering in the parent ion's potential. These scattering interferences have a particular potential for revealing electronic structure and dynamics.

A prominent scattering interference structure is the so-called strong-field photoelectron holography [6,7]. It arises from the interference of two parts of the electron wave packet that are ionized within a fraction of a quarter optical cycle and are subsequently scattered differently in the parent ion's potential [8]. The holographic interference causes spider-leg-like fringes along the laser polarization direction in the photoelectron momentum distribution. This interference structure has been shown to be a powerful tool for probing fundamental strong-field processes [3,5,8–15], valence-shell electronic motion [16], and molecular structure and ultrafast dynamics [17–19] (see also Ref. [20] for a recent review of the topic).

Whereas holographic scattering is most distinct in the middle to high photoelectron momentum range due to the underlying recollision step, the low-momentum region of the photoelectron spectrum is especially affected by Coulomb scattering [21–23]. The observed fanlike interference structure in the lowest momentum range has been shown to reveal orbital symmetry [24] and has been found to originate in soft scattering of electron trajectories within 1/18 of the crest of an

optical cycle [25]. However, in contrast to holographic interferences, the potential of the fanlike low-momentum structure to access ultrafast dynamics remains largely unexplored.

Here, we employ a semiclassical two-step model [5,26] to resolve the subcycle interference of photoelectron wave packets by using a quarter-cycle interference scheme. Particularly, we focus on the fanlike interference structure in the low-momentum region of the photoelectron distribution to unveil its formation mechanism. The disentanglement of this interference structure is accomplished by considering its temporal structure and the Coulomb potential effect from the ion separately. We show that this structure originates in the interference between scattered and unscattered electron wave packets from different direct quarter cycles within a single optical cycle. Furthermore, our analysis reveals that the parent ion's influence on the scattered photoelectron is greatest only a short time after tunneling ionization and well before the moment of closest approach. Hence we believe that this specific structure can resolve ion dynamics on the sub-optical-cycle time scale.

**II. METHOD**

Presently, there are several commonly used models for simulating photoelectron momentum distributions which take the parent ion's Coulomb field into account, such as the Coulomb quantum-orbit strong-field approximation (CQSFA) [27], the quantum-trajectory Monte Carlo (QTMC) model [12,28], and the semiclassical two-step (SCTS) model [5,26]. These models can be categorized into two groups [20]: The CQSFA solves the inverse problem, which means it needs prior knowledge of the electron orbits. The QTMC and SCTS models, on the other hand, solve the direct problem, which means only the initial conditions are needed and the electron orbits are obtained by propagation in time. Due to the simplicity of solving the direct problem, we will use the SCTS model to study the photoelectron momentum distribution in this paper.

\*twang110@uottawa.ca

†andre.staudte@nrc.ca

The semiclassical two-step model treats the strong-field ionization process as two major steps: tunneling ionization and electron trajectory propagation. For the tunneling ionization step, the tunneling ionization rate at ionization time  $t_0$  is determined by the Ammosov-Delone-Krainov (ADK) ionization rate [29]:

$$w_{\text{ADK}}(t_0, v_{\perp}) \simeq \exp\left[-\frac{2\kappa^3}{3|F(t_0)|}\right] \exp\left[-\frac{\kappa v_{\perp}^2}{|F(t_0)|}\right], \quad (1)$$

where  $\kappa = \sqrt{2I_p(t_0)}$ ,  $I_p(t_0)$  is the ionization potential of the atom,  $F(t_0)$  is the instantaneous electric amplitude of the laser field, and  $v_{\perp}$  is the initial transverse velocity of the electron at the tunneling exit point. The tunneling exit point  $r_e$  is calculated using the tunnel ionization in parabolic coordinates with induced dipole and Stark shift (TIPIS) approximation [30]:

$$r_e = \frac{I_p(t_0) + \sqrt{I_p(t_0)^2 - 4\beta_2 F(t_0)}}{2F(t_0)}, \quad \beta_2 = Z - \frac{\sqrt{2I_p(t_0)}}{2}, \quad (2)$$

where  $Z$  is the ionic charge and the Stark-shifted ionization potential is  $I_p(t_0) = I_{p,0} + \frac{1}{2}(\alpha_N - \alpha_I)F(t_0)^2$ , where  $\alpha_N$  and  $\alpha_I$  denote the static polarizability for the atom and the ion, respectively, and  $I_{p,0}$  is the ionization potential without any shifts. In order to simplify the calculation, we have used a two-dimensional model. Then the initial coordinates of a tunneling electron on the  $x$ - $y$  plane can be defined as ( $r_x = r_e, r_y = 0$ ), while the initial velocity of the electron will be  $\mathbf{v}_0 = (v_x = 0, v_y = v_{\perp})$ . Here, we assume that the longitudinal velocity of the photoelectron at the tunneling exit point is zero.

For the electron trajectory propagation step, the tunneled electron will evolve classically within the laser field and the nuclear Coulomb field. The Hamiltonian of the system is  $H(t) = \frac{1}{2}\mathbf{p}^2 + V(\mathbf{r}) + \mathbf{r} \cdot \mathbf{F}(t)$ , where  $V(\mathbf{r})$  is the nuclear potential.  $\mathbf{F}(t) = \hat{\mathbf{e}}_x f(t) \sin(\omega t)$  is the electric field of the laser pulse, and  $\omega$  is the circular frequency. Then the electron motion is described by the canonical equations

$$\frac{d\mathbf{r}}{dt} = \frac{\partial H}{\partial \mathbf{p}}, \quad \frac{d\mathbf{p}}{dt} = -\frac{\partial H}{\partial \mathbf{r}}, \quad (3)$$

where  $H$  is the Hamiltonian of the system and  $\mathbf{p}$  is the momentum vector of the photoelectron.

On its classically calculated path the photoelectron accumulates a phase  $\Phi$ , which is calculated by [26]

$$\begin{aligned} \Phi(t_0, \mathbf{v}_0) = & -\mathbf{v}_0 \cdot \mathbf{r}(t_0) + I_{p,t_0} \\ & - \int_{t_0}^{\tau_f} dt \left\{ \frac{p(t)^2}{2} + V - \mathbf{r}(t) \cdot \nabla V[\mathbf{r}(t)] \right\} \\ & + \Phi_f^C(\tau_f), \end{aligned} \quad (4)$$

where  $\tau_f$  is the duration of the laser pulse and  $V[\mathbf{r}(t)]$  is the ionic Coulomb potential. For a real Coulomb potential,  $V[\mathbf{r}(t)] = -Z/|\mathbf{r}(t)|$ . The asymptotic Coulomb phase  $\Phi_f^C(\tau_f)$  has an analytical form [26]:

$$\Phi_f^C(\tau_f) = -Z\sqrt{b} \left[ \ln g + \operatorname{asinh}\left(\frac{\mathbf{r}(\tau_f) \cdot \mathbf{p}(\tau_f)}{g\sqrt{b}}\right) \right], \quad (5)$$

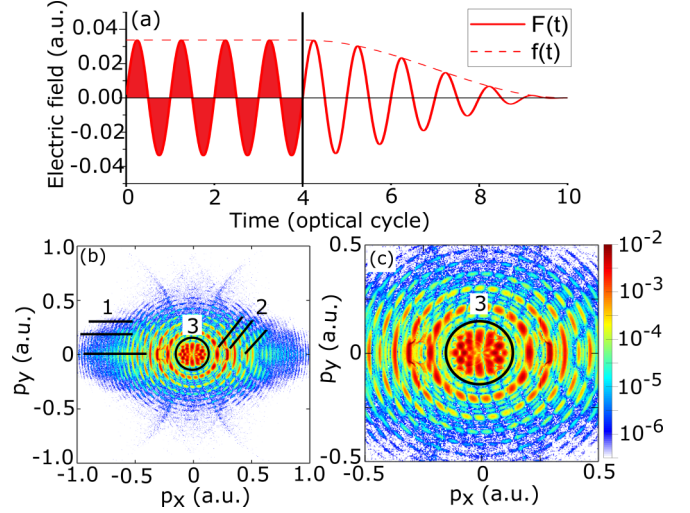


FIG. 1. (a) Electric field of the half-trapezoidal laser pulse. The solid red line is the electric field, and the dashed red line shows its envelope. The red shaded areas indicate the laser cycles where tunneling ionization is allowed. (b) Photoelectron momentum distribution for a H atom ionized by the laser pulse in (a) with wavelength  $\lambda = 2000$  nm and peak intensity  $I = 4 \times 10^{13}$  W/cm<sup>2</sup>. The black lines indicate the strong-field photoelectron holography fringes (labeled “1”) and the temporal double slit fringes (labeled “2”). The black circle labeled “3” indicates the fanlike interference structure in the low-momentum range. (c) Magnification of (b).

where  $b = 1/(2E)$  and  $g = \sqrt{1 + 2EL^2}$ . Here,  $E$  and  $L$  are the electron energy and angular momentum at the end of the laser pulse, respectively.

In this paper, we use a hydrogen atom as the model system to study subcycle photoelectron holography. Thus we set  $Z = 1$ ,  $I_{p,0} = 0.5$  a.u.,  $\alpha_N = 4.5$  a.u. [31], and  $\alpha_I = 0.0$  a.u. In order to study the subcycle photoelectron dynamics independently of the carrier-envelope phase (CEP), a long laser pulse is ideal. Here, we use a laser pulse with a half-trapezoidal envelope, where the first four cycles have a constant field amplitude followed by a cosine squared turnoff over six cycles. We chose the specific form of the pulse envelope to minimize the effect of the CEP on the photoelectron distributions. The wavelength of the laser pulse is 2000 nm, and the peak intensity is  $4 \times 10^{13}$  W/cm<sup>2</sup>. The electric field vector of our laser pulse is along the  $x$  direction, and its field strength versus time is shown in Fig. 1(a).

Our semiclassical two-step model simulation is performed using  $10^9$  electron trajectories. For each trajectory, the ionization time is randomly and uniformly assigned within the laser pulse, and its initial transverse velocity is randomly and uniformly set within an interval of  $(-v_{\perp}^{\max}, v_{\perp}^{\max})$ , where  $v_{\perp}^{\max} = 3(|\mathbf{F}(t_0)|/\sqrt{2I_p(t_0)})^{\frac{1}{2}}$ . After the initial conditions are defined, the Hamiltonian of each tunneling electron is solved by using the symplectic method, which can keep numerical stability for calculations over long time spans [32]. The asymptotic momentum distribution is calculated and recorded on a two-dimensional (2D) momentum grid with  $1000 \times 1000$  bins, coherently adding the ionization rates of all

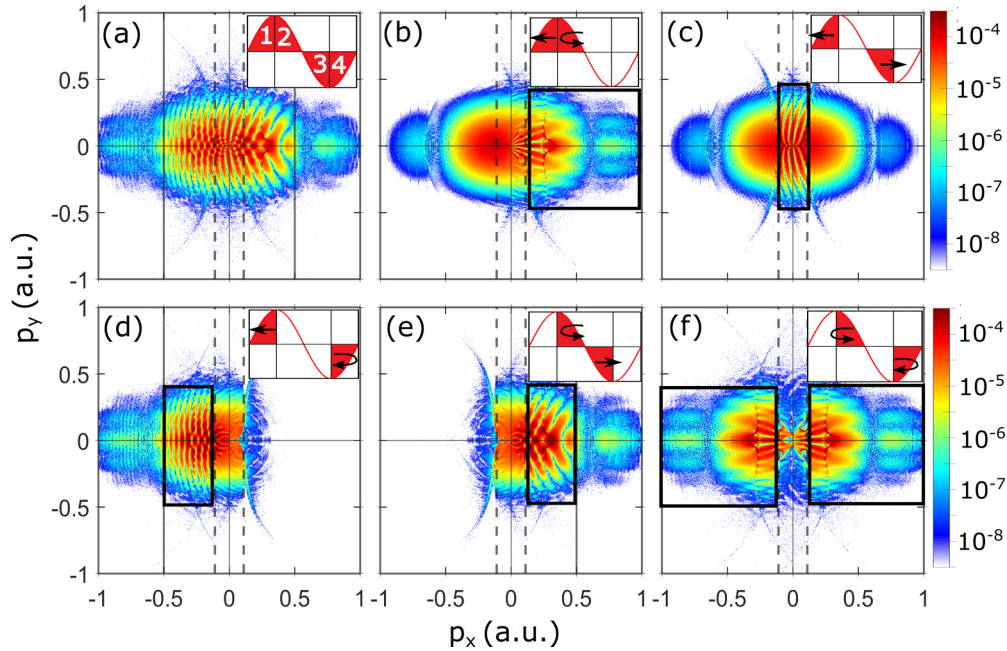


FIG. 2. Photoelectron momentum distributions with ionization restricted to different quarter-cycle (QC) combinations within the first optical cycle of the pulse shown in (a): (a) the complete optical cycle; (b) QCs 1 and 2, forward scattering holography; (c) QCs 1 and 3, low-energy interference structure; (d) QCs 1 and 4, extended temporal double slit; (e) QCs 2 and 3, temporal double slit; and (f) QCs 2 and 4, forward scattering holography. The quarter cycles are labeled as shown in the inset of (a). In (b)–(f), the insets indicate the quarter cycles (solid red) where tunneling ionization is permitted, and the black box indicates the main interference fringes. The straight and curved black arrows in each inset mark the direct and indirect QCs, and their directions mark the momentum directions of electrons ionized within corresponding QCs in the photoelectron momentum distribution.

trajectories:

$$P(\mathbf{k}) = \left| \sum_{j=1}^n \sqrt{w_{\text{ADK}}(t_0^j, \mathbf{v}_0^j)} \exp[i\Phi(t_0^j, \mathbf{v}_0^j)] \right|^2, \quad (6)$$

where  $j$  labels the electron trajectory,  $n$  is the total number of trajectories, and  $\Phi(t_0^j, \mathbf{v}_0^j)$  is the phase of the  $j$ th trajectory.

### III. RESULTS AND DISCUSSION

Figure 1(b) shows the calculated momentum distributions with ionization permitted only during the first four optical cycles of the laser pulse. We can clearly observe the dominant ring structure of the intercycle interference characteristic for above-threshold ionization (ATI). We can also distinguish several intracycle interference structures such as the strong-field photoelectron holography pattern [7], indicated by horizontal black lines (labeled “1”), and the temporal double slit fringes [33], indicated by 45° black lines (labeled “2”). Moreover, a fanlike interference structure [34] can be identified in the low-momentum part, indicated by a black circle (labeled “3”). The low-momentum part has been magnified in Fig. 1(c) to make the fanlike interference structure more visible. As we will show below, the fanlike interference structure (labeled “3”) extends to larger transverse momenta than indicated with the black circle but is obscured by ATI rings for the laser field parameters in Fig. 1.

In experiments, Fourier filtering can be employed to remove the dominant ATI structures and reveal subcycle interference structures [35]. Here, we can simply restrict ionization

to a single optical cycle, thereby removing any intercycle interference. In Fig. 2(a) we show the momentum distribution that is formed when ionization is restricted to the first optical cycle within the envelope in Fig. 1(a). Comparing with Fig. 1(b), the ATI rings are completely absent, and pronounced, vertical interference fringes emerge in the momentum range from  $-0.5$  to  $0.5$  a.u.

In Figs. 2(b)–2(f), we now disentangle the momentum spectrum with respect to the contributions of the different quarter-cycle combinations within a single optical cycle. In each figure the main interference structure is indicated by a black box. Remarkably, the dominant modulations of the single-cycle photoelectron spectrum in Fig. 2(a) can be assigned to just three distinct quarter-cycle pairs, shown in Figs. 2(c)–2(e). Of these structures the ones in Fig. 2(e) can be recognized as the well-known temporal double slit [33,36]. The structure in Fig. 2(d) is a similar, but less known, larger double slit from nonadjacent quarter cycles, which manifests itself in narrower fringes. Finally, the quarter-cycle combination in Fig. 2(c) produces the low-energy vertical fringes. Figures 2(b) and 2(f) show the characteristic holographic fringes parallel to the laser polarization, which are almost indiscernible in the combined distribution [Fig. 2(a)]. Notably, Fig. 2(f) has a deficit of photoelectrons with  $|p_x| < 0.1$  a.u. compared with the other cases.

To understand the lack of low-momentum electrons in Fig. 2(f), it is useful to classify the four quarter cycles by their trajectories. In the simple man’s model of recollision, the electron is treated fully classically, and the long-range Coulomb potential of the parent ion is ignored [37,38]. Within

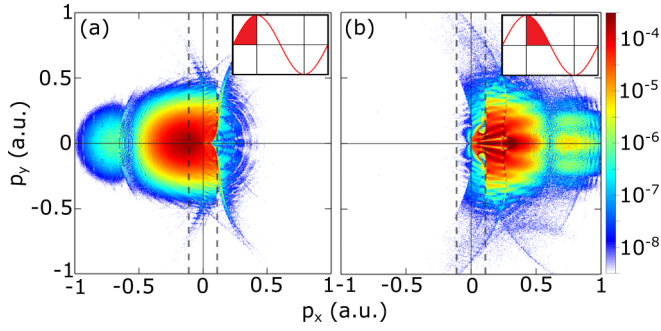


FIG. 3. Photoelectron momentum distributions from direct (a) and indirect (b) quarter cycles. The two black dashed lines indicate  $p_x = -0.1$  a.u. and  $p_x = 0.1$  a.u., respectively. The illustration in the right upper corner of each panel shows the quarter cycle where tunneling ionization happens.

this framework, the first and third quarter cycles [as indicated in Fig. 2(a)] are called *direct* quarter cycles, because the ionized electrons are driven directly away from the ion without a chance for recollision. The second and fourth quarter cycles are called *indirect* quarter cycles, because the ionized electrons are first driven back towards the parent ion, where they can *rescatter* in the ion potential, before traveling to the detector. The photoelectron momentum distributions of a single direct quarter cycle and a single indirect quarter cycle are shown in Fig. 3. Figure 2(f) is the only case without a direct quarter cycle, and thus the lack of low-momentum electrons must be due to rescattering. This can be further demonstrated by comparing the photoelectron momentum distributions of single direct and indirect quarter cycles. It can be seen that in Fig. 3(b) the electrons ionized from an indirect quarter cycle can hardly populate the low-momentum region:  $|p_x| < 0.1$  a.u. compared with that in Fig. 3(a). On the other hand, Fig. 2(c) shows the only combination without an indirect, rescattering quarter cycle, exhibiting interference fringes in the low-momentum region. Such interference requires the electrons ionized within two different direct quarter cycles to achieve overlap in the momentum space. However, this is in contrast to the simple man's model, because the electric fields of the first and third quarter cycles are opposite; hence the ionized electrons within them will fly in different directions and cannot have the same momentum according to the simple man's model. In the following, we will focus on the low-momentum, vertical interference fringes and their origin beyond the simple man's model.

To begin, we introduce a soft-core potential to replace the  $-Z/|\mathbf{r}(t)|$  Coulomb potential in our simulation with a soft-core Coulomb potential  $V[\mathbf{r}(t)] = -\frac{Z}{\sqrt{(|\mathbf{r}(t)|+\beta)^2}}$ , where  $\beta \geq 0$  is the soft-core parameter. A larger  $\beta$  means a shallower potential; thus  $\beta = 0.0$  corresponds to a real Coulomb potential, and  $\beta = \infty$  means no Coulomb potential. Here, we only investigate the effect of the Coulomb potential on the electron propagation after tunneling ionization; the effect of the ionic potential on quantum tunneling will not be considered. Hence the initial coordinates and probability of tunneling electrons will be calculated according to Eqs. (1) and (2). The evaluation of the asymptotic Coulomb phase  $\Phi_f^C(\tau_f)$  uses the real Coulomb potential, because the ionized electron will be at a

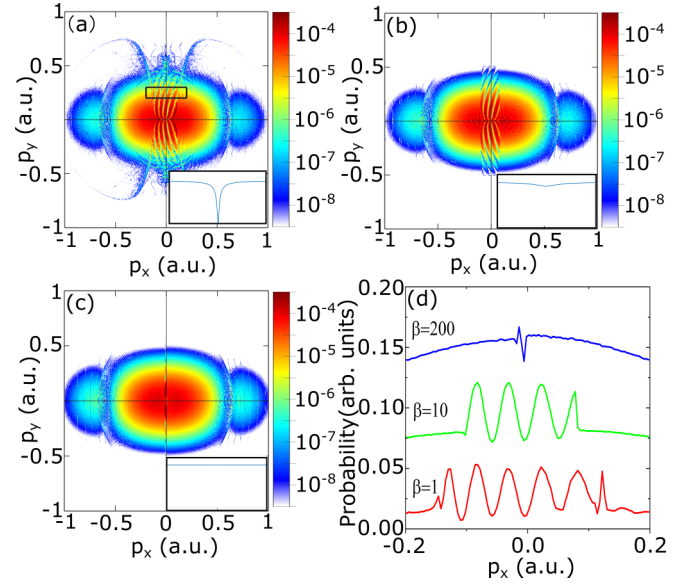


FIG. 4. Photoelectron momentum distributions with ionization restricted to the first and third quarter cycles with different soft-core Coulomb potentials, (a)  $\beta = 1$ , (b)  $\beta = 10$ , and (c)  $\beta = 200$ . (d)  $p_x$  integrated over a small window in  $p_y$ ,  $0.2$  a.u.  $< p_y < 0.3$  a.u. as indicated by the black box in (a). Note that the probability curves for  $\beta = 10$  and  $\beta = 200$  have been shifted upwards by  $0.06$  and  $0.11$ , respectively, for a better visualization. The insets in (a)–(c) sketch the soft-core Coulomb potentials for different  $\beta$ .

large distance from the core at the end of the laser pulse and thus the soft-core parameter  $\beta$  can be neglected.

We now sample the tunneling electrons within the first and third quarter cycles in the ionization step and let the tunneled electrons propagate within the soft-core Coulomb potential. Figure 4 shows the momentum distributions for three different soft-core Coulomb potentials. We can see that a soft-core parameter  $\beta = 1$  [Fig. 4(a)] produces almost identical distributions to a real Coulomb potential [Fig. 2(c)]. However, when  $\beta$  is increased to  $10$ , the number of fringes is reduced as shown in Fig. 4(b). If we further increase  $\beta$  to  $200$ , the low-momentum fanlike structure almost disappears as shown in Fig. 4(c).

Figure 4(d) shows the momentum distributions projected on the  $x$  axis for the three cases within a specific momentum range indicated by a black box in Fig. 4(a). The reduction of the low-momentum interference with increasing  $\beta$  demonstrates that it originates in the ionic potential.

To further understand the formation of the low-momentum interference, we now examine the electron trajectories as a function of  $\beta$ . Figures 5(a) and 5(b) show the time-dependent probability distributions  $P(t, r_x)$  along the light polarization direction for  $\beta = 0$  and  $\beta = \infty$ , respectively. Each figure contains  $10^7$  electron trajectories tunnel ionized during the first direct quarter cycle. After tunnel ionization, the electrons evolve in the combined laser and Coulomb field and form an oscillating cluster of electron trajectories in both cases.

For the real-Coulomb-potential case in Fig. 5(a), the cluster of electron trajectories oscillates and drifts toward the nucleus during its propagation and finally forms an upward propagation trend, indicated by an upward sloping black line. Such a drift

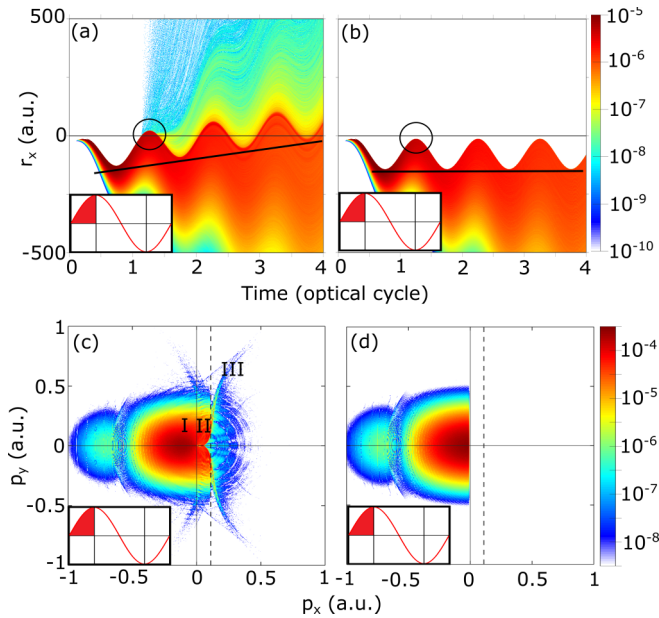


FIG. 5. Electron trajectory (a) and (b) and momentum distributions (c) and (d) from a single, direct quarter cycle. (a) and (c) are for the real-Coulomb-potential case, and (b) and (d) are for the no-Coulomb-potential case. In (c), the labels “I,” “II,” and “III” mark the undrifted, low-momentum drifted, and high-momentum drifted electrons, respectively. The insets indicate the quarter cycles (solid red) where tunneling ionization is permitted. The dashed vertical lines correspond to  $p_x = 0.1$  a.u.

trend also makes it possible for electrons to recollide with the nucleus as indicated by the black ellipse.

For the zero-Coulomb-potential case in Fig. 5(b), the cluster of electron trajectories remains on one side of the nucleus and has a stable propagation trend which is indicated by a horizontal black line. Recollision cannot happen in this case, and a gap between trajectory cluster and nucleus remains, as indicated by the black ellipse. Intuitively, the drift of the electron bunch in the real-Coulomb-potential case is induced by the effect of the parent ion’s Coulomb attraction on the electrons after tunneling ionization.

The electron trajectory drift in position space will also have effect in momentum space. In Figs. 5(c) and 5(d) we compare the momentum distributions with and without Coulomb potential. In the presence of a Coulomb potential [Fig. 5(c)] the photoelectrons populate significantly the positive-low-momentum region, region II ( $0 \text{ a.u.} < p_x < 0.1 \text{ a.u.}$ ), and to a much lesser extent even the positive-mid-momentum region, region III ( $0.1 \text{ a.u.} < p_x < 0.5 \text{ a.u.}$ ). In contrast, in the absence of a Coulomb potential [Fig. 5(d)] all electrons concentrate in the negative momentum range:  $p_x < 0$ .

Based on the above, we classify photoelectrons ionized within a direct quarter cycle as drifted and undrifted electrons. We refer to photoelectrons as undrifted if their final momenta are in the hemisphere allowed by the Coulomb-field-free model [region I in Fig. 5(c)]. Correspondingly, electrons in regions II and III will be called low- and high-momentum drifted electrons, respectively. Moreover, we can see that the high-momentum drifted electrons (region III) form a structure with two long legs which cover a large transverse momentum

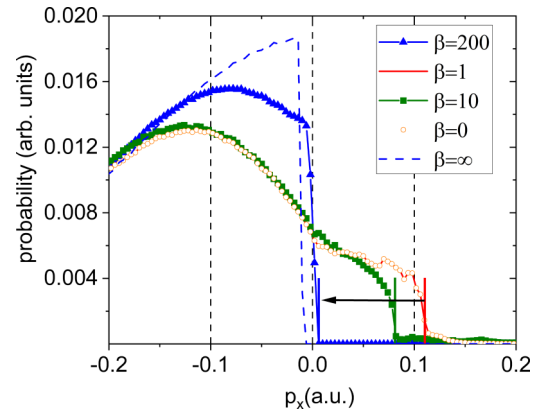


FIG. 6. Parallel momentum distributions of the first quarter cycle for different soft-core Coulomb potentials. Here,  $\beta = \infty$  corresponds to the no-Coulomb-potential case.

range, while for the low-momentum drifted electrons (region II) the transverse momentum remains below 0.5 a.u.

Figure 6 illustrates how the soft-core parameter can gradually shift distribution from region I to regions II and III by plotting the momentum component  $p_x$  parallel to the polarization for several soft-core parameters. It can be seen that all the spectra for  $\beta = 0, 1, 10, 200$  cover at least a part of the positive-low-momentum space below 0.1 a.u. The cutoffs in the low-momentum range, indicated by solid vertical lines, reveal that with increasing parameter  $\beta$ , the low-momentum coverage area decreases from about 0.1 a.u. to near-zero momentum as indicated by the black arrow.

In Fig. 7 we now illustrate how the two direct quarter cycles within one optical cycle contribute to the creation of the low-momentum interferences. Figures 7(a) and 7(b) show

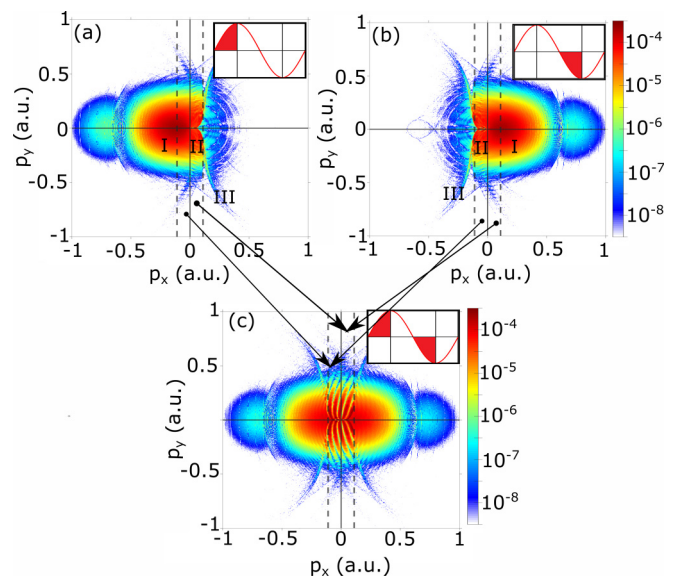


FIG. 7. Illustration of the interference scheme for the formation of the low-momentum fanlike interference structure. (a) and (b) Photoelectron momentum distributions for the first and third quarter cycles, respectively. The labels “I,” “II,” and “III” mark the undrifted, low-momentum drifted, and high-momentum drifted electrons, respectively. (c) Combined photoelectron momentum distribution of the two quarter cycles.

the momentum distributions for  $\beta = 1$ , and the first and third quarter cycles, respectively. Only in the coherent combination of the two quarter cycles shown in Fig. 7(c) does the fanlike interference pattern become visible in the low-momentum region. Notably, the high-momentum drifted electrons in region III do not visibly interfere with the undrifted electrons of the opposite quarter cycle.

Now that we have established that the Coulomb potential plays a key role in the formation of the low-momentum fanlike interference structure through low-momentum drifted electrons, we want to see whether the influence of the Coulomb potential can be correlated with specific parts of the electron trajectory [39]. In order to examine how the Coulomb field affects specific parts of the photoelectron trajectory, we now introduce a time-variable, soft-core Coulomb potential:

$$V(\mathbf{r}) = \frac{-Z}{\sqrt{[r + \beta(t)]^2}}, \quad \begin{cases} \beta = 0, & t < T_c \\ \beta = 200, & t > T_c, \end{cases} \quad (7)$$

where  $T_c$  is defined as the time when the Coulomb potential is effectively turned off by setting a large soft-core parameter  $\beta = 200$ . Here, we choose four values for  $T_{c,n}$ , namely,  $T_{c,n} = 3/4, 1, 3/2,$  and  $2$  optical cycles. In addition, we want to point out that due to the insensitivity of undrifted electrons to the Coulomb potential as shown in Figs. 5(c) and 5(d), such time-dependent Coulomb potential and time partitions allow us to examine the effect of the Coulomb potential on the drifted electrons which are only from one direct quarter cycle.

In Fig. 8(a) we show the trajectories for a fixed  $\beta = 0$  with the four critical times indicated. The chosen values for  $T_c$  divide the third-quarter-cycle trajectories into three different stages: In stage I, the electrons have just been ionized and begin to fly away from the nucleus through the action of the laser field. In stage II, the electrons are slowed down and pulled back towards the nucleus. Finally, in stage III, the electrons have their first return to the parent ion.

Figures 8(b)–8(e) show the distributions of the four times,  $T_{c,n}$ , when the Coulomb field is switched off. Whereas for  $T_{c,1}$  in Fig. 8(b) the negative-momentum part of the low-momentum fanlike interference structure is completely missing, the cases  $T_{c,2}$  [Fig. 8(c)],  $T_{c,3}$  [Fig. 8(d)], and  $T_{c,4}$  [Fig. 8(e)] exhibit an almost identical fanlike interference structure in the low-momentum range. This means that the formation of the low-momentum fanlike interference structure is largely complete before  $T_{c,2}$ . Thus the Coulomb field acts on the electrons just when they begin to fly away from the nucleus within 0.25 optical cycles.

In addition, the variable Coulomb potential allows us to narrow down the time window for the creation of the thin leglike structures [indicated by black ellipses in Figs. 8(d) and 8(e)] that are present in all momentum distributions featuring a Coulomb potential. While the leglike structure is absent before  $T_{c,2}$  [if compared with Figs. 8(b) and 8(c)], a right-sided leg structure has formed by  $T_{c,3}$  [Fig. 8(d)], and it is fully recovered after two full optical cycles [Fig. 8(e)]. Thus, in contrast to the fanlike low-momentum structure, the formation of the high-momentum legs occurs at one full optical cycle after ionization. Specifically, the leglike structures originate

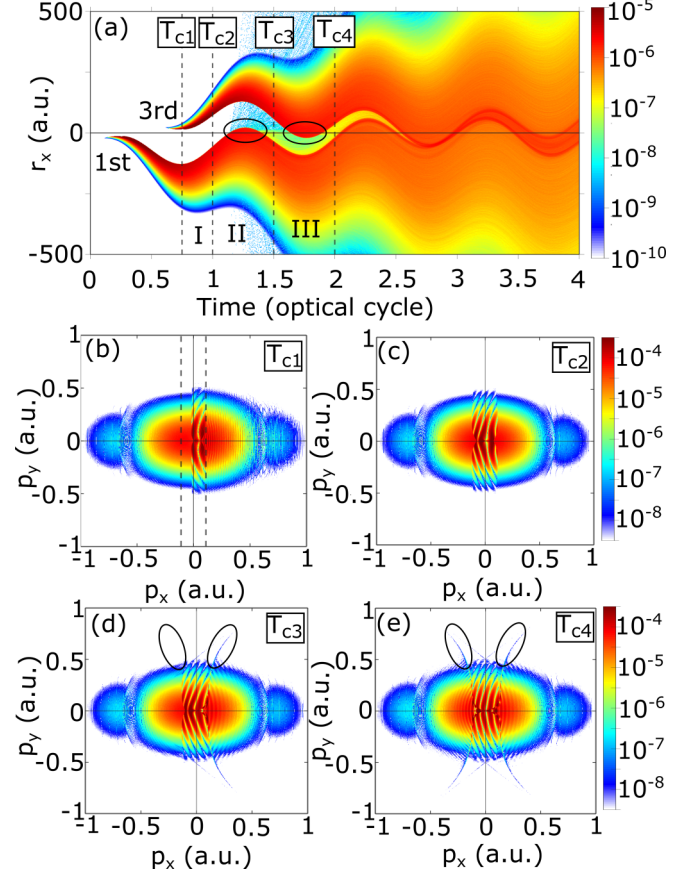


FIG. 8. Time partition of the electron dynamics after tunneling ionization and photoelectron momentum distributions for different critical time. (a) Electron trajectory distribution. The four black dashed lines correspond to times:  $3/4, 1, 3/2,$  and  $2$  optical cycles. The labels “I,” “II,” and “III,” mark the three dynamics stages of the ionized electrons born within the third quarter cycle. The two black ellipses mark where the recollisions happen. (b)–(e) Photoelectron momentum distribution for the four critical times. In (d) and (e), the black ellipses mark the thin leglike structures.

in the large-angle scattering that can occur when the electron returns to the origin [black ellipses in Fig. 8(a)].

#### IV. CONCLUSION

In conclusion, we investigated the photoelectron momentum distributions of strong-field ionization in a 2000-nm laser field using the semiclassical two-step model. First, we disentangled various subcycle interference structures by resolving the contributions from different quarter-cycle combinations within one optical cycle. These distributions revealed several key subcycle interference structures of multiphoton ionization, among them a new extended temporal double slit and a low-momentum interference structure. We then studied the temporal and dynamical origin of the low-momentum interference structure. We found that it is caused by electrons that are born in opposite direct quarter cycles and undergo soft scattering in the parent ion’s Coulomb potential. Our analysis shows that the soft scattering occurs before the first turning point of the electron trajectory. We also identified large-angle (hard) scattering in the trajectories from direct quarter cycles at the moment of closest return.

Our results hold promise for the detection of electronic structure dynamics in the low-energy part of the photoelectron spectrum. Ultrafast postionization dynamics such as spin-orbit wave packets [40], or charge migration [41], cause a change in the ionic charge distribution and thus will leave a signature in the low-energy part of the photoelectron momentum spectrum. Using polarization-gated laser pulses not only will allow us to suppress other, purely symmetry-driven interferences [42] but also will enable ultrafast angular probing of the parent ion's charge distribution.

## ACKNOWLEDGMENTS

The authors gratefully acknowledge support from the Joint Centre for Extreme Photonics of the National Research Council of Canada and the University of Ottawa, and from National Science and Engineering Research Council Discovery Grants No. RGPIN-419092-2013 and No. RGPIN-05858-2020. Y.M. acknowledges support from Deutsche Forschungsgemeinschaft (German Research Foundation) Grant No. MI 2434/1-1.

- 
- [1] R. Gopal, K. Simeonidis, R. Moshhammer, T. Ergler, M. Durr, M. Kurka, K. Kuhnelt, S. Tschuch, C. D. Schroter, D. Bauer, J. Ullrich, A. Rudenko, O. Herrwerth, T. Uphues, M. F. Schultze, E. Goulielmakis, M. Uiberacker, M. Lezius, and M. Kling, Three-Dimensional Momentum Imaging of Electron Wave Packet Interference in Few-Cycle Laser Pulses, *Phys. Rev. Lett.* **103**, 053001 (2009).
- [2] D. G. Arbol, K. L. Ishikawa, K. Schiessl, E. Persson, and J. Burgdorfer, Intracycle and intercycle interferences in above-threshold ionization: The time grating, *Phys. Rev. A* **81**, 021403(R) (2010).
- [3] X.-B. Bian, Y. Huismans, O. Smirnova, K.-J. Yuan, M. J. J. Vrakking, and A. D. Bandrauk, Subcycle interference dynamics of time-resolved photoelectron holography with midinfrared laser pulses, *Phys. Rev. A* **84**, 043420 (2011).
- [4] A. S. Maxwell, A. Al-Jawahiry, T. Das, and C. F. Faria, Coulomb-corrected quantum interference in above-threshold ionization: Working towards multitrajectory electron holography, *Phys. Rev. A* **96**, 023420 (2017).
- [5] N. I. Shvetsov-Shilovski and M. Lein, Effects of the Coulomb potential in interference patterns of strong-field holography with photoelectrons, *Phys. Rev. A* **97**, 013411 (2018).
- [6] M. Spanner, O. Smirnova, P. Corkum, and M. Ivanov, Reading diffraction images in strong field ionization of diatomic molecules, *J. Phys. B: At. Mol. Opt. Phys.* **37**, L243 (2004).
- [7] Y. Huismans, A. Rouzée, A. Gijsbertsen, J. Jungmann, A. Smolkowska, P. Logman, F. Lépine, C. Cauchy, S. Zamith, T. Marchenko, J. Bakker, G. Berden, B. Redlich, A. van der Meer, H. Muller, W. Vermin, K. Schafer, M. Spanner, M. Ivanov, O. Smirnova *et al.*, Time-resolved holography with photoelectrons, *Science* **331**, 61 (2011).
- [8] G. Porat, G. Alon, S. Rozen, O. Pedatzur, M. Krüger, D. Azoury, A. Natan, G. Orenstein, B. Bruner, M. Vrakking, and N. Dudovich, Attosecond time-resolved photoelectron holography, *Nat. Commun.* **9**, 2805 (2018).
- [9] D. D. Hickstein, P. Ranitovic, S. Witte, X.-M. Tong, Y. Huismans, P. Arpin, X. Zhou, K. Keister, C. Hogle, B. Zhang, C. Ding, P. Johnsson, N. Toshima, M. J. J. Vrakking, M. M. Murnane, and H. C. Kapteyn, Direct Visualization of Laser-Driven Electron Multiple Scattering and Tunneling Distance in Strong-Field Ionization, *Phys. Rev. Lett.* **109**, 073004 (2012).
- [10] M. Meckel, A. Staudte, S. Patchkovskii, D. Villeneuve, P. Corkum, R. Dörner, and M. Spanner, Signatures of the continuum electron phase in molecular strong-field photoelectron holography, *Nat. Phys.* **10**, 594 (2014).
- [11] M. Li, X. Sun, X. Xie, Y. Shao, Y. Deng, C. Wu, Q. Gong, and Y. Liu, Revealing backward rescattering photoelectron interference of molecules in strong infrared laser fields, *Sci. Rep.* **5**, 8519 (2015).
- [12] X. Song, C. Lin, Z. Sheng, P. Liu, Z. Chen, W. Yang, S. Hu, C. D. Lin, and J. Chen, Unraveling nonadiabatic ionization and Coulomb potential effect in strong-field photoelectron holography, *Sci. Rep.* **6**, 28392 (2016).
- [13] M.-M. Liu, M. Li, C. Wu, Q. Gong, A. Staudte, and Y. Liu, Phase Structure of Strong-Field Tunneling Wave Packets from Molecules, *Phys. Rev. Lett.* **116**, 163004 (2016).
- [14] S. G. Yu, X. Y. Lai, Y. L. Wang, S. P. Xu, L. Q. Hua, W. Quan, and X. J. Liu, Photoelectron holography from multiple-return backscattering electron orbits, *Phys. Rev. A* **101**, 023414 (2020).
- [15] Y. Zhou, J. Tan, M. Li, and P. Lu, Probing the launching position of the electron wave packet in molecule strong-field tunneling ionization, *Sci. China Phys. Mech. Astron.* **64**, 273011 (2021).
- [16] M. He, Y. Li, Y. Zhou, M. Li, W. Cao, and P. Lu, Direct Visualization of Valence Electron Motion Using Strong-Field Photoelectron Holography, *Phys. Rev. Lett.* **120**, 133204 (2018).
- [17] X.-B. Bian and A. D. Bandrauk, Attosecond Time-Resolved Imaging of Molecular Structure by Photoelectron Holography, *Phys. Rev. Lett.* **108**, 263003 (2012).
- [18] L. Chen, C. Huang, X. Zhu, P. Lan, and P. Lu, Molecular photoelectron holography by an attosecond XUV pulse in a strong infrared laser field, *Opt. Express* **22**, 20421 (2014).
- [19] M. Haertelt, X.-B. Bian, M. Spanner, A. Staudte, and P. B. Corkum, Probing Molecular Dynamics by Laser-Induced Backscattering Holography, *Phys. Rev. Lett.* **116**, 133001 (2016).
- [20] C. F. de Morrison Faria and A. Maxwell, It is all about phases: ultrafast holographic photoelectron imaging, *Rep. Prog. Phys.* **83**, 034401 (2020).
- [21] C. Blaga, F. Catoire, P. Colosimo, G. Paulus, H. Muller, P. Agostini, and L. DiMauro, Strong-field photoionization revisited, *Nat. Phys.* **5**, 335 (2009).
- [22] W. Quan, Z. Lin, M. Wu, H. Kang, H. Liu, X. Liu, J. Chen, J. Liu, X. T. He, S. Chen, H. Xiong, L. Guo, H. Xu, Y. Fu, Y. Cheng, and Z. Z. Xu, Classical Aspects in Above-Threshold Ionization with a Midinfrared Strong Laser Field, *Phys. Rev. Lett.* **103**, 093001 (2009) [*Phys. Rev. Lett.* **103**, 119901(E) (2009)].
- [23] T.-M. Yan, S. V. Popruzhenko, M. J. J. Vrakking, and D. Bauer, Low-Energy Structures in Strong Field Ionization

- Revealed by Quantum Orbits, *Phys. Rev. Lett.* **105**, 253002 (2010).
- [24] X. Y. Lai, S. G. Yu, Y. Y. Huang, L. Q. Hua, C. Gong, W. Quan, C. F. Faria, and X. J. Liu, Near-threshold photoelectron holography beyond the strong-field approximation, *Phys. Rev. A* **96**, 013414 (2017).
- [25] X. Song, M. Zhu, X. Liu, H. Zhang, W. Jia, Q. Xue, C. Lin, W. Quan, J. Chen, X. Liu, and W. Yang, Low-energy interference structure with attosecond temporal resolution, *J. Phys. B: At. Mol. Opt. Phys.* **54**, 144003 (2021).
- [26] N. I. Shvetsov-Shilovski, M. Lein, L. B. Madsen, E. Rasanen, C. Lemell, J. Burgdorfer, D. G. Arbo, and K. Tokesi, Semiclassical two-step model for strong-field ionization, *Phys. Rev. A* **94**, 013415 (2016).
- [27] A. Maxwell, A. Jawahiry, X. Lai, and C. Faria, Analytic quantum-interference conditions in coulomb corrected photoelectron holography, *J. Phys. B: At. Mol. Opt. Phys.* **51**, 044004 (2018).
- [28] M. Li, J. W. Geng, H. Liu, Y. Deng, C. Wu, L. Y. Peng, Q. Gong, and Y. Liu, Classical-Quantum Correspondence for Above-Threshold Ionization, *Phys. Rev. Lett.* **112**, 113002 (2014).
- [29] M. Ammosov, N. Delone, and V. Krainov, Tunnel ionization of complex atoms and of atomic ions in an alternating electromagnetic field, *Sov. Phys. JETP* **64**, 1191 (1986).
- [30] A. Pfeiffer, C. Cirelli, M. Smolarski, D. Dimitrovski, M. Abusamha, L. Madsen, and U. Keller, Attoclock reveals natural coordinates of the laser-induced tunnelling current flow in atoms, *Nat. Phys.* **8**, 76 (2012).
- [31] K. McDowell, Exact static dipole polarizabilities for the excited  $S$  states of the hydrogen atom, *J. Chem. Phys.* **65**, 2518 (1976).
- [32] X. Liu, Y. Qi, J. He, and P. Ding, Recent progress in symplectic algorithms for use in quantum systems, *Commun. Comput. Phys.* **2**, 1 (2007).
- [33] M. Richter, M. Kunitski, M. Schöffler, T. Jahnke, L. Schmidt, M. Li, Y. Liu, and R. Dörner, Streaking Temporal Double-Slit Interference by an Orthogonal Two-Color Laser Field, *Phys. Rev. Lett.* **114**, 143001 (2015).
- [34] C. Maharjan, A. Alnaser, I. Litvinyuk, P. Ranitovic, and C. Cocke, Wavelength dependence of momentum-space images of low-energy electrons generated by short intense laser pulses at high intensities, *J. Phys. B: At. Mol. Opt. Phys.* **39**, 1955 (2006).
- [35] N. Werby, A. Natan, R. Forbes, and P. H. Bucksbaum, Disentangling the subcycle electron momentum spectrum in strong-field ionization, *Phys. Rev. Research* **3**, 023065 (2021).
- [36] F. Lindner, M. Schätzel, H. Walther, A. Baltuška, E. Goulielmakis, F. Krausz, D. Milošević, D. Bauer, W. Becker, and G. G. Paulus, Attosecond Double-Slit Experiment, *Phys. Rev. Lett.* **95**, 040401 (2005).
- [37] P. B. Corkum, Plasma perspective on strong field multiphoton ionization, *Phys. Rev. Lett.* **71**, 1994 (1993).
- [38] F. Krausz and M. Ivanov, Attosecond physics, *Rev. Mod. Phys.* **81**, 163 (2009).
- [39] S. P. Goreslavski, G. G. Paulus, S. V Popruzhenko, and N. I. Shvetsov-Shilovski, Coulomb Asymmetry in Above-Threshold Ionization, *Phys. Rev. Lett.* **93**, 233002 (2004).
- [40] M. Kübel, Z. Dube, A. Naumov, D. Villeneuve, P. Corkum, and A. Staudte, Spatiotemporal imaging of valence electron motion, *Nat. Commun.* **10**, 1042 (2019).
- [41] F. Calegari, A. Trabattini, A. Palacios, D. Ayuso, M. Castrovilli, J. Greenwood, P. Declève, F. Martín, and M. Nisoli, Charge migration induced by attosecond pulses in bio-relevant molecules, *J. Phys. B: At. Mol. Opt. Phys.* **49**, 142001 (2016).
- [42] R. P. Sun, Y. L. Wang, Y. Zhou, S. G. Yu, S. P. Xu, X. Y. Lai, W. Quan, and X. J. Liu, Precise control of intracycle interference with a phase-stabilized polarization-gated laser pulse, *Phys. Rev. A* **105**, L021103 (2022).